Multiscale Bi-Gaussian Filter for Adjacent Curvilinear Structures Detection With Application to Vasculature Images

Changyan Xiao, Marius Staring, Yaonan Wang, Denis P. Shamonin, and Berend C. Stoel

***Abstract*— The intensity or gray-level derivatives have been widely used in image segmentation and enhancement. Conventional derivative filters often suffer from an undesired merging of adjacent objects because of their intrinsic usage of an inappropriately broad Gaussian kernel; as a result, neighboring structures cannot be properly resolved. To avoid this problem, we propose to replace the low-level Gaussian kernel with a bi-Gaussian function, which allows independent selection of scales in the foreground and background. By selecting a narrow neighborhood for the background with regard to the foreground, the proposed method will reduce interference from adjacent objects simultaneously preserving the ability of intraregion smoothing. Our idea is inspired by a comparative analysis of existing line filters, in which several traditional methods, including the vesselness, gradient flux, and medialness models, are integrated into a uniform framework. The comparison subsequently aids in understanding the principles of different filtering kernels, which is also a contribution of this paper. Based on some axiomatic scale-space assumptions, the full representation of our bi-Gaussian kernel is deduced. The popular γ-normalization scheme for multiscale integration is extended to the bi-Gaussian operators. Finally, combined with a parameter-free shape estimation scheme, a derivative filter is developed for the typical applications of curvilinear structure detection and vasculature image enhancement. It is verified in experiments using synthetic and real data that the proposed method outperforms several conventional filters in separating closely located objects and being robust to noise.**

***Index Terms*— Bi-Gaussian kernel, curvilinear structure detection, feature extraction, multiscale filtering, vessel enhancement.**

I. Introduction

DETECTING curvilinear structures, often simply called lines or tubes, in digital images is an important low-level operation of computer vision that has many applications. In medical imaging, the detection of tubes like blood vessels or airways, is usually a prior step for quantification of diseases and evaluation of therapy progress [1]. Curvilinear structures are also frequently seen in industry. For example, printing and packaging workers perform quality control of their products by (automatically) counting the number of linear stripes in a photograph of a stack of sheets [2], see also Figure 4. However, accurate detection of curvilinear structures is not easy due to the complexity of an inhomogeneous background and noise. Especially in the presence of disturbance from adjacent objects, the task will become more challenging. Note that the issue of adjacency is relative to various imaging configurations, e.g. a limited resolution compared to the distance between objects, can be considered a main obstacle for vessel separation in medical images.

There are many techniques for curvilinear structure detection reported in the literature, and a recent survey can be found in [3]. Among them, the derivative filters have drawn much attention. Since the seminal work of Koller [4], the image derivatives were frequently utilized to detect either boundaries or centerlines of tubular objects. Usually, we consider the boundaries as odd or antisymmetric structures, which only respond to the first-order intensity or gray-level derivatives. From this, the structure tensor method [5] was adopted to determine the local boundary direction and strength. On the other hand, centerlines are typically even or symmetric structures and should be detected with the second-order derivatives. Correspondingly, the popular Hessian line filters [6]–[8] just aim to find the tube centers. Originating from [9], the medialness tube filter [10] is a hybrid method, which depends on the Hessian to find axial directions and the boundary gradient to estimate local diameters. To account for size variation, the filters generally identify objects at multiple scales and combine all results into a single response based on some normalization scheme [11]. Behind these methods, a Gaussian (linear) scale space is often employed to calculate the spatial intensity derivatives. As well-known, Gaussian smoothing is equal to an isotropic diffusion that may result in blurring across object boundaries, and will inevitably cause closely located objects to merge together. Therefore, traditional derivative filters are unsuitable for detection of adjacent structures.

Several efforts have been made to remedy this shortcoming. McAuliffe et al. [12] defined an adaptive multi-local medialness to improve centerline detection. Instead of the traditional radially symmetric Gaussian function, they used the

Manuscript received November 16, 2011; revised June 22, 2012; accepted August 13, 2012. Date of publication August 31, 2012; date of current version December 20, 2012. This work was supported in part by National Science Foundation of China under Grant 61172160 and Grant 60835004, the SRF for ROCS, SEM under Grant [2011] 1139, the NSF of Hunan Province under Grant 12JJ9019, and the FRF for the Central Universities of China. The associate editor coordinating the review of this manuscript and approving it for publication was Prof. Sina Farsiu.

C. Xiao and Y. Wang are with the College of Electrical and Information Engineering, Hunan University, Changsha 410082, China (e-mail: C.Xiao@hnu.edu.cn; yaonan@hnu.cn).

M. Staring, D. P. Shamonin, and B. C. Stoel are with the Division of Image Processing, Department of Radiology, Leiden University Medical Center, Leiden 2300 RC, The Netherlands (e-mail: M.Staring@lumc.nl; D.P.Shamonin@lumc.nl; B.C.Stoel@lumc.nl).

Color versions of one or more of the figures in this paper are available online at http://ieeexplore.ieee.org.

Digital Object Identifier 10.1109/TIP.2012.2216277

first derivative of a bivariate Gaussian to make boundariness measurements, where shape and orientation of the filtering kernel can be adaptively adjusted to minimize adjacent disturbances. With additional homogeneity and symmetry constraints, the modified medialness filters [13], [14] are able to reduce influence from sparsely neighboring structures, but their effect might be limited when handling background with serious inhomogeneity. Implemented in an iterative scheme, the Perona-Malik model [15] and edge-enhancing anisotropic diffusion [16] can efficiently prevent the interregion smoothing based on some edge-tuned conductance functions. However, the leaking through weak boundaries and local scale optimization still remain a challenge. Recently, Bauer and Bischof [17] presented a novel tube detecting approach, which depends on the gradient vector flow (GVF) [18] to extend the gradient around boundaries into tube centers. Calculating the shape likelihood directly on the regularized vector field, their method efficiently avoids the multi-scale computation, and allows detection of centerlines independent of tube size and neighborhood background. The drawbacks of GVF are its heavy computing cost and the sensitivity to intensity variation arising from very local gradient calculation. Following the isotropic gradient flux [19], Law and Chung [20] proposed an optimally oriented flux (OOF) to distinguish orientational difference of tubular structures. Their model was verified to be robust against disturbance induced by close objects, and have been successfully applied to vessel segmentation and anisotropic enhancement [21], [22].

In this paper, we present a novel filtering kernel for detection of closely located structures. Our idea originates from a comparative analysis and reformulation of existing line filters. By directly merging two Gaussians with different parameters, the proposed bi-Gaussian (BG) kernel allows independent selection of scales on foreground and background. By taking a narrow neighborhood during the derivative computation, our method helps to minimize adjacent disturbances, but does not sacrifice the homogeneity constraint inside object regions. To develop the kernel as a general detector, its full analytical representation is deduced and the traditional γ-normalization scheme for linear scale space operators is extended here to meet the requirement of multi-scale integration. Specifically, combining with a parameter-free shape measure, a typical application is to improve the extraction of adjacent tubular objects such as vasculature or the edges of stacked sheets.

The remainder of the paper is organized as follows. We first retrospect on the traditional line filters in Section II. Then, the bi-Gaussian kernel is proposed in Section III. Section IV introduces a shape measure and the multi-scale integration scheme. The experiment results with synthetic and real images are given in Section V, and Section VI is the conclusion.

II. Retrospection on Traditional Filters

In this section, several traditional line or tube filters are reviewed. To investigate and understand the inherent drawbacks of existing filters, we will show that these methods as well as the proposed bi-Gaussian kernel can fit into a unified framework by reformulating them from the viewpoint of differential convolution [23]. This will then help in developing a new solution to the adjacent structure problem.

Consider a low-pass filter $f(\sigma, x) = I(x) * h(\sigma, x)$, with h being the smoothing kernel at scale σ and $I(x)$ the original image. The derivatives of response function f often work as structure detectors in image analysis. According to the differentiation property of convolution, the i-th order derivative in the direction $\vec{r}$ can be calculated with

$$\partial^i f(\sigma, x)/\partial \vec{r}^i = I(x) * \partial^i h(\sigma, x)/\partial \vec{r}^i. \quad (1)$$

Although implemented by convolution with varying kernels, the second-order derivative operators for 2D or 3D image structures detection are divided into two main types: Laplacian and Hessian, which essentially combine the 1D directional derivatives of Eq. (1) in different ways. Usually, to account for the variation of object sizes, the filters are merged with a multi-scale framework, where a scale normalizing term $NF(\sigma)$ is often multiplied, i.e. the normalized derivative is defined as $NF(\sigma) \cdot \partial^i f(\sigma, x)/\partial \vec{r}^i$ for interscale compatibility. As an overall description, several representative filters are listed in Table I and their scale normalization factors are particularly included. Since there might be two different scale variables involved in the filters, we adopt σ to denote the main foreground scale and σ_b the background or small gradient scale.

The following sections describe several popular filters used for curvilinear structure detection. We will show that all these methods can be written as a differential convolution filter like Eq. (1), but with different definitions of the underlying filtering kernel $h(\sigma, x)$. This paper is focused on the kernel, rather than the complete filter. Here, the kernel means the $h(\cdot)$ and its derivatives in Eq. (1), whereas a complete filter might include other auxiliary components such as the shape estimating function, scale and orientation integration or combination of derivative operators.

A. Gaussian Line Filters

The traditional Gaussian line filters, often known as vesselness methods [6]–[8], are among the most widely used line filters. They essentially depend on the orientational difference or anisotropic distribution of the second-order directional derivatives $\partial^2 I_\sigma/\partial \vec{r}^2 = \vec{r}^t H_\sigma(x)\vec{r}$ to define a tube shape measure, where $\vec{r}$ indicates the unit vector and H_σ the Hessian at scale σ. Under a linear scale space [24], [25], the term is equivalent to $\partial^2 I_\sigma/\partial \vec{r}^2 = I(x) * \partial^2 G(\sigma, x)/\partial \vec{r}^2$, i.e. convoluting with a directional Derivative of Gaussian (DoG). On the other hand, by radially rotating the DoG to define an isotropic kernel, Fritsch et al. [26] developed a central medialness filter for extraction of anatomic objects with nonparallel sides in medical images. Neglecting the orientational difference, their scheme actually employed a multi-scale Laplacian of Gaussian (LoG) operator like [27]. In both filters, the scale normalization factor $NF(\sigma)$ was set to σ^2.

One inherent weakness of Gaussian kernels is that they may smooth across object boundaries, and tend to merge closely located structures together. This can be explained from a 1D curve of the second-order DoG kernel in Fig. 1g, where a big

TABLE I
SUMMARIZING THE DERIVATIVE FILTERS FOR TUBE DETECTION

Method	Article	Filtering Kernel	Derivative Operator	$NF(\sigma)$
LoG	Fritsch [26]	Gaussian	Laplacian	$\sigma^{2\gamma}$
Vesselness	Lorenz [6], Frangi [8], Sato [7] etc.	Gaussian	Hessian	$\sigma^{2\gamma}$
Flux	Vasilevskiy and Siddiqi [19]	Rectangle	Laplacian	σ^{γ}
OOF	Law and Lung [20], Benmansour [22]	Rectangle	Hessian	σ^{γ}
Medialness	Krissian [10]	Gaussian and Rectangle	3D Hessian and 2D Laplacian	$\sigma^{2\gamma}$
BG	this paper	Bi-Gaussian	Hessian	$\sigma^{2\gamma}$

*Here, the default value of parameter $\gamma = 1$.

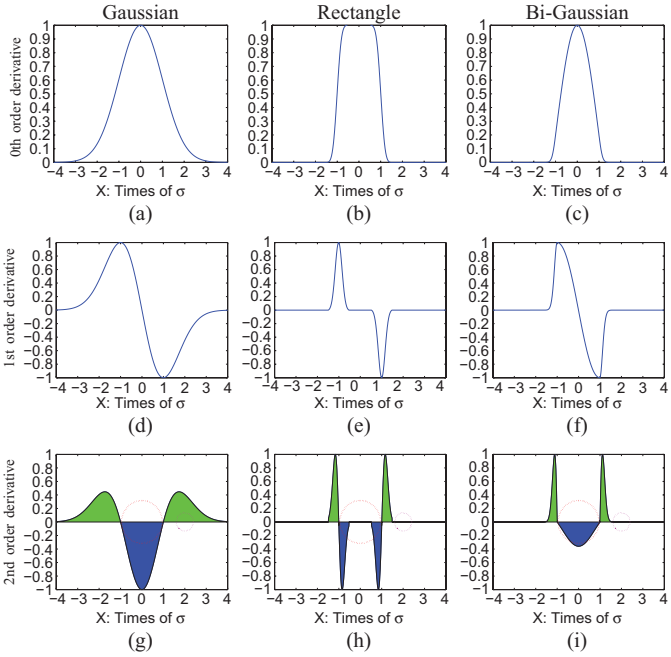

Fig. 1. Comparison of different kinds of filtering kernels, including Gaussian, rectangular, and bi-Gaussian kernels. (a)–(c) Original kernel functions. (d)–(f) First-order derivatives. (g)–(i) Second-order derivatives. Here, the magnitudes of all the kernels are normalized to 1 for comparison. The x coordinates are represented in multiples of scale σ, and $\sigma_b = 0.16\sigma$ is adopted for illustration of rectangular and bi-Gaussian kernels. Subfigures at the bottom row: big circles denote cross sections of desired tubular objects and the smaller circles denote the adjacent disturbances.

circle is used to represent the cross-section of the main tube and the small dotted circle a nearby disturbing object. As seen, although the scale of *DoG* is consistent with the tube radius, the disturbing object is undesirably covered by the side lobes of the kernel and thus will inevitably lead to a wrong response.

B. Gradient Flux Models

The flux-based tube filter was first introduced for vessel segmentation by Vasilevskiy and Siddiqi [19]. The image gradient flux is a discrete implementation of the gradient divergence represented as a surface integral of gradient ∇I projected along the surface normal $\vec{n}$. As elaborated in Appendix A, its mathematical expression can be transformed to

$$Flux(\sigma, x) = \sigma \cdot I(x) * \Delta \bar{R}(\sigma, \sigma_b, x) \tag{2}$$

with σ the spherical radius and $\bar{R}(\sigma, \sigma_b, x) = G(\sigma_b, x) * \bar{R}(\sigma, x)$ being a smoothened rectangle function. Obviously, the gradient flux model can be considered a convolution filter with a Laplacian of Rectangle (LoR) kernel.

Recently, the flux filter was further improved by Law and Chung [20]. In spite of a different theoretical background, their Optimally Oriented Flux (OOF) model defined a second-order matrix $Q_{\sigma,x}$ with components

$$q^{i,j}_{\sigma,x} = \sigma \cdot I(x) * \partial^2 \bar{R}(\sigma, \sigma_b, x)/\partial x_i \partial x_j. \tag{3}$$

As presented, $Q_{\sigma,x}$ is equal to a Hessian matrix calculated with partial differentials of $\bar{R}(\sigma, \sigma_b, x)$ namely DoR. In OOF, σ_b is fixed to 1 and σ is multiplied for scale normalization as the flux model.

Compared with the traditional Gaussian line filters, a salient advantage of flux models is their better performance in separating adjacent objects [20]. This can be investigated from the 1D curve of the smoothened rectangle kernel shown in Fig. 1h, where only a small neighborhood (width defined by σ_b) around the object boundary is taken into account by the second-order DoR operator. On condition $\sigma_b < \sigma$, it is obvious that a narrow selection of concerned regions between the object (the big circle) and its background helps to reduce the influence from adjacent structures (the small circle). However, the good performance is obtained at the cost of relaxing the homogeneity constraint inside object regions, which might make it subject to false responses in the presence of intensity inhomogeneity and noise. Note that the rectangle kernel specifically denotes the smoothened rectangle kernel in this paper, since a pure rectangle kernel is non-differentiable and seldom directly used as a derivative operator.

C. Medialness Filters

The medialness concept was originally presented by Pizer et al. [9] to evaluate the likelihood that a point belongs to the medial axis of an object. Krissian et al. [10] developed an adaptive offset medialness function for 3D vessel detection. The function is said to be adaptive in that the orientation of the filter kernel is locally adapted by the eigenvectors $\vec{e}_1$ and $\vec{e}_2$, which correspond to the two major principal curvatures of Hessian matrix. The meaning of "offset" is that the boundary information at points equidistant to the tube center is measured. The medialness function $M(x)$ was defined at a scale σ_b in proportion to the vessel radius σ, i.e. $\rho = \sigma_b/\sigma$

is constant. As described in Appendix B, we can reformulate it to

$$M(\sigma, \sigma_b, x) = \sigma^{\gamma+1} \cdot I(x) * \Delta \bar{R}^c(\sigma, \sigma_b, x) \tag{4}$$

where $\bar{R}^c$ corresponds to a 2D smoothened rectangle kernel through the transverse plane. The γ is a scale-normalizing coefficient often optimized to 1, but a smaller value (0.75) was actually used by the original authors in real vessel images. Therefore, the above medialness definition is equivalent to an isotropic 2D LoR response.

As a hybrid method, the medialness filter depends on the 3D Gaussian kernel $G(\sigma, x)$ to find the vascular orientation, which is also subject to adjacent interferences. Moreover, although the 2D medialness helps to locate vessel boundaries more accurately, the inherent drawback of rectangle kernels might cause intraregion discontinuities being detected wrongly, like in the gradient flux models.

III. Proposed Method

Motivated by the retrospection and reformulation of traditional line detecting filters, we present a bi-Gaussian filtering kernel in this section. Our innovations focus on designing the low-level kernel function, and the related scale-normalization scheme will also be investigated. In Section III-A we propose the general shape of the bi-Gaussian kernel and the idea behind this. Section III-B lists conditions adopted from scale-space theory, which are needed to completely define the bi-Gaussian kernel. This derivation is done in Section III-C. A comparison of the related kernels in the frequency domain is given in Section III-D. Section III-E extends the kernel to a multi-scale framework, and an extension to dimensions higher than 1 is given in Section III-F.

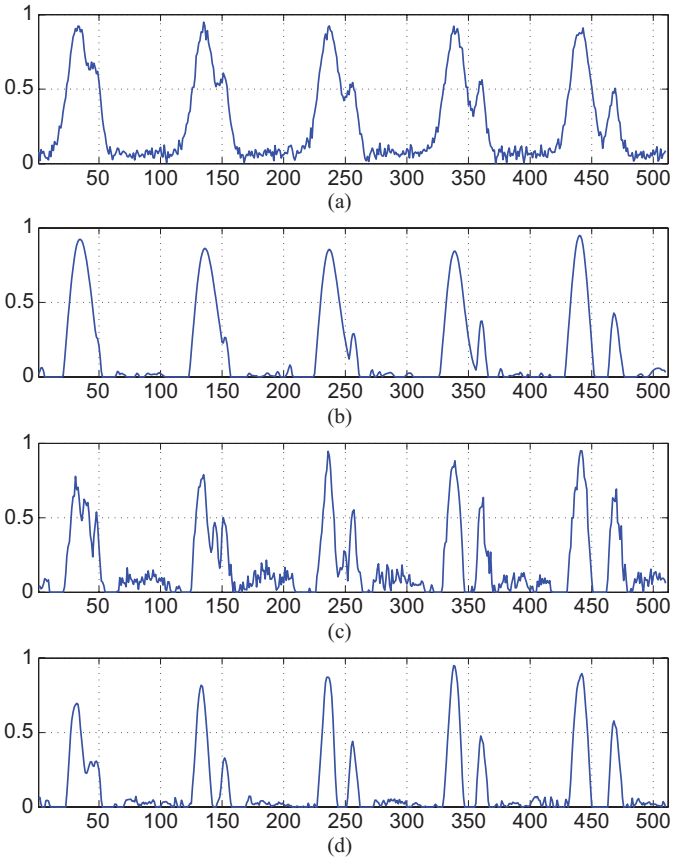

Fig. 2. Testing the 1-D second-order derivatives on the basis of different kernels with a synthetic signal. The magnitudes of response curves are all normalized to [0, 1) for convenience of comparison. A scale ratio $\sigma_b/\sigma = 0.2$ is used for the bi-Gaussian kernel. (a) Original image. (b) Gaussian kernel. (c) Rectangle kernel. (d) Bi-Gaussian kernel.

A. Defining a New Second-Order Derivative

As introduced in Section II, the Gaussian kernels and their derivatives hold an attractive property in noise suppression, but suffer from disturbances induced by adjacent structures. The reason is that they adopt a single scale on both foreground and background. For instance, when the size of objects increases, the Gaussian function $G(\sigma, x)$ has to use a bigger σ to adapt to the change. Thus, it simultaneously increases the possibility of introducing more interference, since a wider neighborhood will be sampled.

Conversely, the rectangle kernels $\bar{R}(\sigma, \sigma_b, x)$ behind flux models have an advantage in separating closely located objects, which is ascribed to the fact that they only depend on the width of the rectangle or main scale σ to conform with the object size, but use a smaller gradient scale σ_b for contrast computation (see Fig. 1h). However, due to the limited boundary and its close neighborhood taken in derivative computation, the interior regions of objects are actually ignored since their weights are set to zero. Consequently, local discontinuities will tend to be exaggerated or the boundaries belonging to different objects might be wrongly identified as an object. In other words, the rectangle kernel only works in situations where the object intensity is assumed to be uniform in advance.

To give an intuitive understanding, the Gaussian and rectangle kernels based second-order derivatives, i.e. $G''(\sigma, x)$ and $\bar{R}''(\sigma, \sigma_b, x)$, are respectively tested with a synthetic signal, where adjacent peaks with different extents of overlap are included and simulated noise was added as shown in Fig. 2a. The signal is convolved with different kernels according to Eq. (1) to detect the two 4- and 8-pixels half width peaks, using the Gaussian, smoothened rectangle and proposed bi-Gaussian kernel in Fig. 1g, h, and i, respectively. Convolution is performed in a multi-scale fashion using the normalization schemes according to Table I and $\sigma \in \{2, 4, 6, 8, 10\}$ pixels. As observed, the left two peak pairs are totally merged under the Gaussian kernel, while false peaks appear in the result of the rectangle kernel.

To remedy the shortcomings of conventional methods, a novel filtering kernel is desired. Based on the previous analysis, our work starts from designing a new second-order derivative, which is critical to the detection of symmetric structures. A straightforward solution is to combine the merits of Gaussian and rectangle kernels, which could be implemented by directly linking the middle negative part of $G''(\sigma, x)$ and the side positive parts of $\bar{R}''(\sigma, \sigma_b, x)$. However, considering the clarity of physical meaning and easiness to understand, instead of $\bar{R}''(\cdot)$ we employ another second-order Gaussian $G''(\sigma_b, x)$,

which is shifted at the object boundaries $x = \pm\sigma$ to approximate the rectangle kernel components. Thus, a piecewise continuous bi-Gaussian function is obtained:

$$BG''(\sigma, \sigma_b, x) = \begin{cases} k \cdot G''(\sigma_b, x - \sigma_b + \sigma), & x \le -\sigma \\ G''(\sigma, x), & \|x\| < \sigma \\ k \cdot G''(\sigma_b, x + \sigma_b - \sigma), & x \ge \sigma. \end{cases} \quad (5)$$

Here, the coefficient k is used to balance the positive and negative weights and its value will be derived later. As shown in Fig. 1i, the new bi-Gaussian operator allows for independent selection of scales (σ and σ_b) on foreground and background.

To verify the new operator, a preliminary test on the synthetic signal is shown in Fig. 2d. From the response curve, it can be found that the proposed method integrated the advantages of both Gaussian and rectangle derivatives, where the majority of adjacent peaks have been efficiently and clearly separated.

B. Constraint of Prior Conditions

As a multi-scale method, the above derivative filters are closely related to scale space theory [24], [25]. Although at this point we can not prove that the bi-Gaussian kernel in Eq. (5) will generate a well-posed scale space, most of the conditions behind the scale-space framework [28], [29] can still be imposed on it. This will help to develop an exact definition of our filtering kernel.

As presented in previous works, we first introduce the constraints of rotation, translation and zoom (scale) invariances, since there are usually no preferred direction, position and size in real images. Then, considering the efficiency of computation, a linear invariance is imposed to guarantee a convolution implementation. Without loss of generality, we use $h(\sigma, x)$, $h'(\sigma, x)$ and $h''(\sigma, x)$ to represent the zero-, first- and second-order kernels, respectively. Usually, the first-order kernel is an odd operator and only detects the anti-symmetrical structures like step-edges, while the even second-order kernel is responsible for symmetrical structures, e.g. the ridge-like tube centerline. This implicitly contains an assumption that $h(\sigma, x)$ is differentiable at least up to the second-order, since higher order derivatives are seldom used in real image analysis. The assumption is also a basic requirement from differential structure detection.

From the above explanation, several conditions can be induced to regulate the kernel definition. Similar axioms or prior assumptions have been used by other authors [30], [31]. For simplification, we adopt a 1D representation as follows.

1) The zero-order kernel $h(\sigma, x)$ works as a smoothing operator, should be a rapidly decreasing function with its bandwidth determined by the scale σ. This is to restrict the blurring or weighted average within an adjustable neighborhood.
2) $h(\sigma, x)$ is integrable, otherwise convolution would not be well-defined.
3) According to rotation invariance, we have $h(x) = h(-x)$, i.e. $h(\sigma, x)$ is an even function.
4) The first-order kernel $h'(\sigma, x)$ is odd with $h'(-x) = -h'(x)$, and the integral $\int_{-\infty}^{+\infty} h'(\sigma, x)dx = 0$. This condition ensures that the first-order operators only respond to antisymmetric objects and neglect constant offset or even structures.
5) Correspondingly, the second-order kernel $h''(\sigma, x)$ is even and its integral $\int_{-\infty}^{+\infty} h''(\sigma, x)dx$ is also 0. This caters to the detection of symmetric objects, and makes the kernel not respondent to both constant components and antisymmetric structures.

It is not difficult to verify that both the Gaussian and rectangle kernel satisfy the listed conditions.

C. Deduction of the Bi-Gaussian Kernels

To exploit the capability of the Hessian matrix in orientation and shape discrimination, it is necessary to derive a full representation of the bi-Gaussian kernel. This is done by integrating Eq. (5).

According to condition 5 above, we first have $\int_{-\infty}^{+\infty} BG''(\sigma, \sigma_b, x)\, dx = 0$ and get

$$k = -\frac{\int_0^{\sigma} G''(\sigma, x)dx}{\int_{\sigma}^{+\infty} G''(\sigma_b, x+\sigma_b-\sigma)dx} = \frac{\sigma_b^2}{\sigma^2}. \quad (6)$$

From condition 4, $BG'(\sigma, \sigma_b, 0)$ should be 0 to ensure its antisymmetry. Then, the analytical formulation of $BG'(x)$ is

$$\begin{aligned} BG'(\sigma, \sigma_b, x) &= \int_0^x BG''(\sigma, \sigma_b, x)dx + BG'(\sigma, \sigma_b, 0) \\ &= \begin{cases} k \cdot G'(\sigma_b, x - \sigma_b + \sigma), & x \le -\sigma \\ G'(\sigma, x), & \|x\| < \sigma \\ k \cdot G'(\sigma_b, x + \sigma_b - \sigma), & x \ge \sigma. \end{cases} \end{aligned} \quad (7)$$

Finally, we derive the zero-order kernel as

$$\begin{aligned} BG(\sigma, \sigma_b, x) &= \int_0^x BG'(\sigma, \sigma_b, x)dx + BG(\sigma, \sigma_b, 0) \\ &= \begin{cases} k \cdot G(\sigma_b, x - \sigma_b + \sigma) + c_1, & x \le -\sigma \\ G(\sigma, x) + c_0, & \|x\| < \sigma \\ k \cdot G(\sigma_b, x + \sigma_b - \sigma) + c_1, & x \ge \sigma. \end{cases} \end{aligned} \quad (8)$$

Here, c_0 and $c_1 = G(\sigma, \sigma) - k \cdot G(\sigma_b, \sigma_b) + c_0$ are offset constants. Based on condition 1, we have $\lim_{x\to\infty} BG(x) = 0$. Thus,

$$c_0 = k \cdot G(\sigma_b, \sigma_b) - G(\sigma, \sigma) = \frac{e^{-1/2}}{\sqrt{2\pi}}\left(\frac{\sigma_b}{\sigma} - 1\right)\frac{1}{\sigma} \quad (9)$$

and $c_1 = 0$. Obviously, $BG(x)$ has even symmetry as demanded by condition 3.

To link the two different scales of bi-Gaussian kernels, we introduce a parameter $\rho = \sigma_b/\sigma$ to represent the scale ratio. Generally, $\rho < 1$ is required for detection of adjacent structures. When $\rho = 1$, the bi-Gaussian kernel will degenerate to a Gaussian. However, the exact selection of ρ is application dependent, since a smaller ρ will benefit the isolation of adjacent interferences, but a bigger one is better for suppression of background noise.

In conclusion, the analytical formula of the proposed kernel have been fully derived. As shown in Fig. 1, the corresponding curves appear to be a fusion between those of the Gaussian and rectangle kernels.

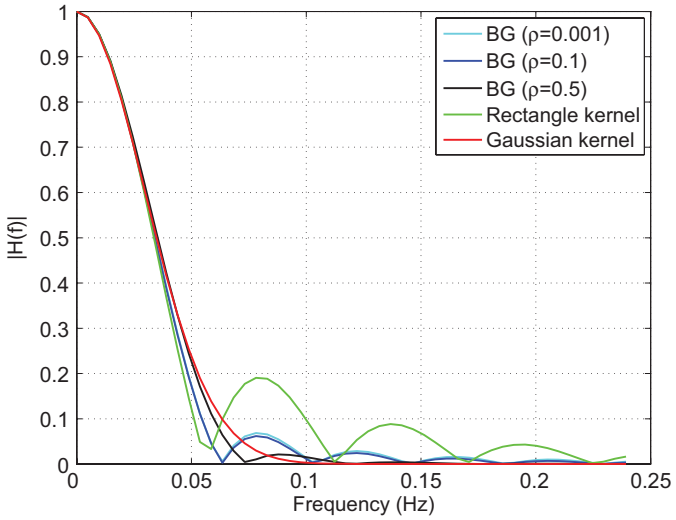

Fig. 3. Comparison of the three kernels in frequency domain. BG: bi-Gaussian kernel.

D. Frequency Domain Analysis

Like the Gaussian and rectangle kernels, the bi-Gaussian kernel is essentially a low-pass filter with the smoothing extent being controlled by the scale parameters. A frequency analysis may provide a qualitative understanding from the viewpoint of traditional signal processing. As well known, the Fourier transformation of a Gaussian function maintains the same Gaussian form, while the pure rectangular function corresponds to a sinc function in the frequency domain, and the Fourier transformation of smoothened rectangle kernels will take the sinc-like shape accordingly. To compare the bi-Gaussian (BG) with the two classic kernels, we plotted their single-sided amplitude spectrums in Fig. 3. As shown, under the same 3db bandwidth, the smoothened rectangle kernel obtains an ideal sharp cut-off at the cost of producing ripples in higher frequencies; the Gaussian kernel efficiently avoids ringing by taking a smooth transition and simultaneously leads to an undesired boundary blurring. Considering the inherent link between object scale and space domain frequency, e.g. a larger scale results in a lower cut-off frequency, a sharp transition of low-pass filters will then help to minimize the mutual interference of neighboring scales. This indirectly explains the advantage of the rectangle kernel on adjacent vessel separation. However, the involved ripples are considered the main cause of high-frequency artifacts in filtering responses, which can be easily found in Fig. 2c and Fig. 5e.

The bi-Gaussian kernel appears to balance well between the cons and pros of Gaussian and rectangle kernels by taking a sharp transition with acceptable ripples. Particularly, the smoothing and ringing extent can be adjusted with the parameter ρ. For example, a larger $\rho = 0.5$ tends to generate a curve more like the Gaussian, while a smaller $\rho = 0.1$ more approximates the rectangle kernel. As shown by the curve of $\rho = 0.001$, the bi-Gaussian kernel will not approach the smoothened rectangle kernel as ρ approaches 0 and suffers far less from ripples.

E. Scale Normalization

In multi-scale filtering, scale normalization is an essential step to guarantee the compatibility of operators at different scales. The popular γ-normalized derivative [11] was originally developed under a linear scale space, and has not been proven applicable to non-Gaussian filters like the rectangle or bi-Gaussian kernels. In this section, we will show that the bi-Gaussian kernel can also be employed in a multi-scale scheme with scale normalization according to the γ-normalization theory. Based on conservation of responses to idealized signals, the normalization criteria are introduced as follows.

1) Constant conservation: it is a basic rule that a smoothing filter should not change a constant function, which is also known as "volume conservation" in the textbook of image processing [32]. Thus, it is forced that the integral $A_0^h = \int_{-\infty}^{+\infty} h(\sigma, x)dx = 1$.
2) Step conservation: the step or Heaviside function $u(x)$ is an ideal antisymmetrical signal. The first-order kernels at different scales should respond equally to it, and we have that the positive half integral $A_1^h = \int_{-\infty}^{0} h'(\sigma, x)dx = -\int_{0}^{+\infty} h'(\sigma, x)dx$ remains unchanged with σ.
3) Bar conservation: As previous authors [3], [10] have done, we adopt a bar or rectangular function $Bar(\sigma, x)$ to represent the idealized profile of tubes like vessels. Since the second-order kernel works as an even operator, it is reasonable to require $h''(\sigma, x)$ preserving a constant response to the bar function at the corresponding scale σ. Then, the positive half integral $A_2^h = 2\int_{\sigma}^{+\infty} h''(\sigma, x)dx = -\int_{-\sigma}^{\sigma} h''(\sigma, x)dx$ should be kept constant.

To realize the interscale compatibility, we multiply the original kernels with a scale-related coefficient NF_i^h ($i = 0$, 1 or 2), i.e. the normalized i-th order derivative is defined as $NF_i^h(\sigma) \cdot \partial^i h(\sigma, x)/\partial x^i$. From the above criteria, the $NF_i^h(\sigma)$ terms can be obtained.

Since the bi-Gaussian kernel $BG(\sigma, x)$ is not originally normalized like a probability density function, a zero-order coefficient $NF_0^{bg}(\sigma)$ is first multiplied to ensure constant conservation, i.e.

$$A_0^{bg} = NF_0^{bg}(\sigma) \cdot \int_{-\infty}^{+\infty} BG(\sigma, \sigma_b, x)dx = NF_0^{bg}(\sigma) \cdot \left[\mathrm{erf}\left(\frac{1}{\sqrt{2}}\right) + \frac{2e^{-1/2}}{\sqrt{2\pi}}\left(\frac{\sigma_b}{\sigma} - 1\right) + \left(1 - \mathrm{erf}\left(\frac{1}{\sqrt{2}}\right)\right)\frac{\sigma_b^2}{\sigma^2}\right] \doteq 1 \tag{10}$$

where $\mathrm{erf}(x)$ indicates the error function. If assuming $\sigma_b \ll \sigma$ or the ratio $\rho = \sigma_b/\sigma$ being fixed, NF_0^{bg} will take a constant value to satisfy Eq. (10). Since a multiplied constant coefficient does not affect the determination of response conservation, NF_0^{bg} will be omitted in the following derivation for simplification. In the paper, a fixed ρ is preferred. Then, for the first-order kernel, we have

$$A_1^{bg} = -NF_1^{bg}(\sigma) \cdot \int_{0}^{+\infty} BG'(\sigma, \sigma_b, x)dx = \frac{1}{\sqrt{2\pi}}(1 - e^{-1/2} + e^{-1/2}\rho)\frac{1}{\sigma} \cdot NF_1^{bg}(\sigma) \tag{11}$$

and $NF_1^{bg}(\sigma) = \sigma$ is chosen according to the step conservation criterion. Further, to satisfy the bar conservation criterion, the positive half integral of the second-order kernel

$$\begin{aligned} A_2^{bg} &= -NF_2^{bg}(\sigma) \cdot \int_{-\sigma}^{\sigma} BG''(\sigma, \sigma_b, x)dx \\ &= \tfrac{2e^{-1/2}}{\sqrt{2\pi}} \tfrac{1}{\sigma^2} \cdot NF_2^{bg}(\sigma) \end{aligned} \tag{12}$$

should be independent of σ. Therefore, the coefficient $NF_2^{bg}(\sigma)$ is chosen σ^2.

From the above deduction, it is obvious that the γ -normalization can be extended to the bi-Gaussian kernels on the condition that the scale ratio $\rho = \sigma_b/\sigma$ is fixed. Actually, our normalizing criteria are also applicable to the Gaussian kernel, and the same result as Pauwels et al. [30] will be derived. As another example, the normalization of rectangle derivatives are elaborated in Appendix C. One additional contribution is that the confusion about scale-normalization (i.e. the different choice of σ or σ^2) between the medialness and flux models [3] is then clarified.

F. Extension to Higher Dimensions

Although the filtering kernels were analyzed mainly with 1D forms in the previous subsections, the extension to high-dimension space is straightforward. For example, by replacing x with the polar radius r equal to the square root of $\sum x_i^2$, the 2D or 3D bi-Gaussian kernel can be easily obtained as $BG(\sigma, \sigma_b, r)$.

As introduced before, the Laplacian and the Hessian are the two common second-order derivative operators. Under the bi-Gaussian kernel, the isotropic Laplacian might be calculated by directly convoluting with $BG''(\sigma, \sigma_b, r)$. However, in order to investigate the orientation and shape information of structures behind the directional derivatives, the anisotropic Hessian should be considered. In the latter case, we first convolve the image with the zero-order kernel $BG(\sigma, \sigma_b, r)$, then the matrix components are separately calculated with

$$\begin{aligned} h_{ij}^{bg}(\sigma, x) &= \sigma^{2\gamma} \cdot I_{x_i x_j}^{bg}(\sigma, x) \\ &= \sigma^{2\gamma} \cdot \partial^2 [BG(\sigma, \sigma_b, r) * I(x)]/\partial x_i \partial x_j. \end{aligned} \tag{13}$$

Here, the normalization coefficient γ is usually assigned a default value 1. Obviously, the Laplacian can also be derived from this equation by summing only the diagonal components.

IV. Multiscale Curvilinear Structures Detection

In Section II, we have verified that several classic line or vessel filters can be integrated into the same differential convolution framework. However, these methods not only have a different underlying kernel, but also employ the kernel in different ways. This makes it difficult to evaluate the performance and influence of various kinds of kernels. To address this issue, we will define a single parameter-free anisotropic (Hessian-based) measure for complex 3D linear or tubular shapes like vessels in this section. The corresponding isotropic Laplacian-based measure, or its 2D implementation, can be easily modified from this definition. Then in the experiments we only need to change the kernel, while keeping the measure fixed.

To describe 3D linear shapes, several popular tubeness or vesselness functions [6]–[8] exist, which depend on the distribution of Hessian eigenvalues to generate a likelihood estimation. Assuming the eigenvalues λ_i ($i = 1, 2, 3$) are sorted in order, e.g. $|\lambda_3| \geq |\lambda_2| > |\lambda_1|$, a bright tubular structure will have $\lambda_1 \approx 0$ with its eigenvector corresponding to the axial direction, and $\lambda_3 \approx \lambda_2 < 0$ with their eigenvectors defining the cross-section plane. Since our main purpose is to verify the performance of different kernels rather than constructing a general segmentation algorithm, the shape estimating scheme of [7] will be followed, but their empirical parameters are removed to make the comparison as fair as possible. Then, a simplified line estimation is defined as

$$\ell(\sigma, x) = \begin{cases} -\frac{\lambda_2}{\lambda_3} \cdot (\lambda_2 + \lambda_3), & \sum_{i=1}^{3} \lambda_i < 0 \\ 0, & \text{otherwise.} \end{cases} \tag{14}$$

Here, the sum of all eigenvalues quantifies the local contrast, which will take a negative response for bright objects [33]. We choose the two eigenvalues inside the transverse plane to measure the structure strength, which approximates the 2D medialness response [10] as analyzed in Eq. (B1), and the eigenvalue ratio is multiplied to punish deviation from the tubular center. By omitting the λ_1 related term, the filter tends to preserve axial continuity, since the intensity variation in this direction is then neglected. From Eq. (14), it is trivial to obtain a similar estimation for the dark tubes, where the eigenvalues take inverse signs. Although the shape measure is defined the same for different filters, the Hessian can be computed in multiple ways, using the Gaussian, rectangle and bi-Gaussian kernels.

To account for the variety of tube sizes, a typical multi-scale integration scheme is utilized to get the optimal response, i.e.

$$\ell_m(x) = \max\{\ell(\sigma, x), \sigma_{\min} < \sigma < \sigma_{\max}\} \tag{15}$$

where $\sigma_{\min}$ and $\sigma_{\max}$ are the minimum and maximum scales. Thus, $\ell_m(x)$ acts like a lineness function, which measures the likelihood of a voxel belonging to a curvilinear structure.

V. Experiments and Validation

In this section, we will compare the bi-Gaussian kernel based filters with conventional methods in experiments by using synthetic and real images. The related algorithm implementation and validation are also introduced. Since the main purpose is to verify the advantage of the proposed kernel over the two classic Gaussian and rectangle kernels, we will keep the filtering framework unchanged but correspondingly adjust the underlying kernel.

Two recent methods including the Laplace-Gabor filter [27] and the gradient vector field (GVF) model [17] are also compared. Note that these methods do not fit the framework of Eq. (1) and Table I, but have been reported with good properties in separating adjacent vessels. Since these models are quite different methods compared to our kernel-based filter, we only simply applied them in the following real image experiments for reference.

A. Algorithm Implementation

Unlike the Gaussian kernel, the proposed bi-Gaussian kernel has no separability property, meaning that the high-dimension convolution cannot be efficiently implemented with a cascade of 1D filters. Instead, we utilize the Fourier convolution theorem to do the computation: the image is Fourier transformed and multiplied with the transformed convolution kernel, then transformed back using the inverse Fourier transform. In our implementation, the fast Fourier transform (FFT) algorithm is adopted for acceleration. Thus, the convolution filter response is calculated with

$$f(x) = \mathcal{FFT}^{-1}\{\mathcal{FFT}[I(x)] \cdot \mathcal{FFT}[h(x)]\} \qquad (16)$$

where $h(x)$ could be one of the bi-Gaussian and rectangle or even the Gaussian kernels. Recently, a similar scheme has been used by Law and Chung [34] in a flux model. According to their report, equivalent computing accuracy can be achieved, while the speed is drastically higher than the traditional spatial domain algorithms.

Currently, our algorithm was implemented in Matlab (MathWorks Inc.) and its embedded FFT library is adopted. The calculation time with Eq. (14) for a typical 256^3 size 3D dataset is about 50s for a single scale on our computer, configured with 2.66 GHz CPU and 3 GB memory. The computing speed is expected to increase largely with a better optimization like in [34] or parallel programming.

The codes of the Laplace-Gabor and GVF filters were downloaded through internet from the home pages of the original authors [18], [27]. Due to the complexity of 3D Gabor transformation, only the 2D version of Laplace-Gabor filter was implemented. Both 2D and 3D implementations of GVF models have been verified with the same public data as in [17].

B. Synthetic Data Experiment

As shown in Fig. 4, a synthetic volume image was generated by merging two tubes with radius 4 and 8 pixels, and the overlap between each tube pair was adjusted by changing their center distance. The intensity profiles were assumed to be in Gaussian distribution, and Gaussian random noise with 16% variance was added to simulate a real environment. Actually, the data is a 3D counterpart of the signal in Fig. 2a.

Here, we first adopted the isotropic Laplacian operator, which is equivalent to replacing the shape function $l(\sigma, x)$ in Eq. (14) by the inverse sum of all Hessian eigenvalues, to verify the performance of various kernels. For the Gaussian and rectangle kernels, the filters then correspond to the existing multi-scale *LoG* [26] and gradient flux models [19], respectively. We set the range of scale σ to 2-10 voxels and uniformly divided it into 5 steps. A fixed σ_b equal to 1 voxel was used for the rectangle kernel as the paper [20], and the ratio parameter ρ of the bi-Gaussian kernel is set to 0.2. All scale normalizing coefficients were configured with default values as in Table I. According to Eq. (15), the multi-scale responses were obtained and are shown in Fig. 4.

As observed, the Gaussian kernel generated the smoothest result among the three kernels, and the intensity distribution through the transverse planes is close to the ground truth,

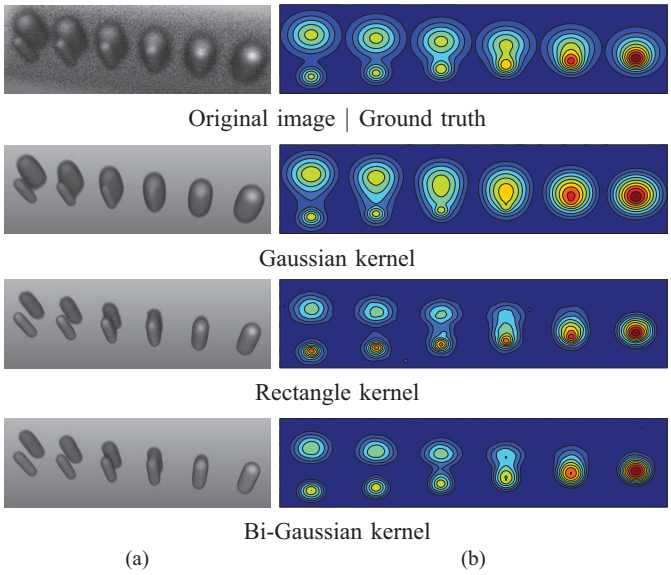

Fig. 4. 3-D synthetic image filtering with different kernels. (a) 3-D visualization. (b) Contours of 2-D cross sections located at the axial midpoint.

but almost all of the tube pairs appear to merge together. The rectangle or flux filter improved the adjacent structures detection while introducing some irregular transitions around the object boundaries. Particularly, the original circular shape of level-contours is frequently distorted, which will make it a problem to localize the centerline or estimate the tube diameter. The bi-Gaussian kernel retains a clear gap between the neighboring tubes, except for the seriously overlapping ones on the right side of the figure. Moreover, the intensity distribution is well preserved as seen from the contour plot. The distinctive advantage is ascribed to an integration of previous kernels, where the intra-region smoothing of Gaussian and the neighborhood adjusting ability of rectangle kernels are seamlessly merged into a single filter. However, both the bi-Gaussian and rectangle kernels appear to sharpen the smooth boundaries, and the tubes are perceived thinner partially due to the selected threshold.

C. Real Data Experiments

1) 2-D Page Images: To compare the filtering kernels in real applications, we first adopt a 2D page image from packaging industry used for sheet-counting, where the data are captured by scanning the sides of a book or paper-stack with CCD cameras for quality control [2], [35]. Fig. 5a shows a typical image with closely located curvilinear structures. Due to noise and background inhomogeneity, it is difficult to directly identify the page stripes. Instead, multi-scale derivative filters are often adopted for preprocessing enhancement. The enhanced image is subsequently used for automatic page-counting, where we mainly employ a peak detection algorithm [36] to locate the sheet centers and then output the number of pages. In the experiment, the scale range is commonly set to 3-6 pixels and 5 steps are used. The ratio ρ of bi-Gaussian kernel is 0.2, and the σ_b of the rectangle kernel is 1 pixel as in [20]. The normalization factors of all the kernels are configured

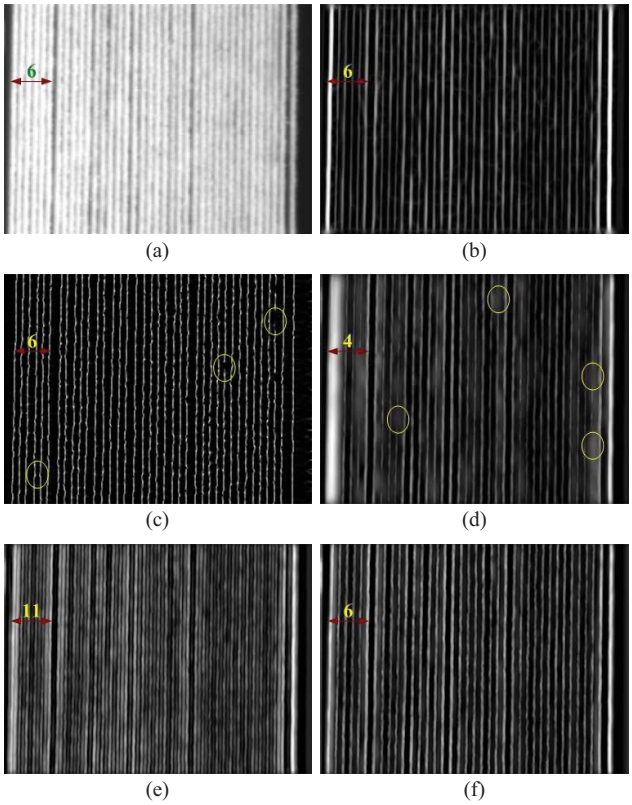

Fig. 5. 2-D page image filtering. (a) Original image. (b) Laplace-Gabor filtering. (c) GVF filtering. (d)–(f) Results from Gaussian, rectangle, and bi-Gaussian kernels, respectively. Yellow digits: detected number of pages in the region denoted by the red arrows, using the algorithm described in [36].

according to Table I. During multi-scale integration, only the Hessian eigenvalue with largest magnitude at each scale, i.e. $l(\sigma, x) = -\lambda_2$ is used to generate the final response. By neglecting the smaller eigenvalue in the axial direction, the continuity along page edges will be better preserved as detailed in Section IV. This is also a requirement from the page-counting task, where the traverse separation and the longitudinal connection are both emphasized. Additionally, a Laplace-Gabor filter [27] and a 2D GVF filter [17], [18] were also applied here and the filtering parameters were optimized to the data.

From the filtering result, the Gaussian kernel seems to blur across weak boundaries, which can be seen from the missed line segments labeled with yellow ellipses in Fig. 5d. Simultaneously, the widened bright stripe on the left just indicates the incorrect merging of adjacent lines. As marked by the red arrows in Fig. 5e, the rectangle kernel leads to an over-estimation of stripe number, which originated from a wrong division of tube regions due to the lack of a homogeneity constraint. However, the overall performance of the bi-Gaussian kernel is better. As shown in Fig. 5f, all stripes have been clearly separated leading to accurate page counting. The Laplace-Gabor filter is comparable to and even better than the bi-Gaussian one with smoother stripes in Fig. 5b. The computing time was however much longer (about 45 times of the bi-Gaussian kernel in our experiments) due to the complexity of Gabor decomposition. The special effect of GVF model is given in Fig. 5c, where the tubes were obviously thinned with highlighting centerlines. As marked with yellow circles, a potential drawback is that the axial gray-level variation has been improperly exaggerated and thus causes some obvious discontinuities or merging of adjacent stripes.

2) 3-D Clinical Images: The filtering kernels are further tested with 3D blood vessel images. We used a time-of-flight MRA image from an open dataset [37] with an image resolution of $0.513 \times 0.513 \times 0.8\ mm^3$. As shown in Fig. 6a, a sub-volume was specifically selected from the "Normal082" sample. In the image, many tangential vessels exist, which have been considered a problem to conventional vessel detecting algorithms [38]. Before filtering, an interpolation algorithm was applied to transfer the image into a $0.5 \times 0.5 \times 0.5\ mm^3$ isotropic data, which is necessary to satisfy the Nyquist criteria during differential convolutions [7].

Considering the complexity of 3D vessels, we utilized a fully defined lineness function in Eq. (14) to generate a multi-scale response on the MRA image. The selected scale range was 1-3 pixels and uniformly divided into 5 steps. All the scale-normalizing coefficients for the Hessian calculation in Eq. (13) were configured according to Table I. The scale ratio ρ of bi-Gaussian kernel was set to 0.1. Since the 3D implementation of Laplace-Gabor filter [27] is not available, we only adopted the GVF model [17] using the same lineness function as the kernel-based filters and the default parameter ($\mu = 0.1$) was verified to be an optimal configuration here.

In the experiment, we focused on the detection of closely located structures. As seen from Fig. 6, the Gaussian kernel failed to distinguish almost all the neighboring vessels due to its over-smoothness. The rectangle kernel was able to separate parallel vessels as the green arrow indicates, but seems quite limited in detecting the cross tangential vessels marked with red arrows. The bi-Gaussian kernel performed much better than the previous two filters concerning all kinds of vessels. The axial continuity and many weak vessels invisible to the traditional filters were well preserved. The GVF method was good in separating adjacent vessels, especially with a merit to detect very weak objects, see the blue arrow in Fig. 6b. However, the axial discontinuity arising from too local gradient estimation was also very obvious just like its 2D counterpart in Fig. 5c. To illustrate the influence of binarizing thresholds, various isosurfaces of the bi-Gaussian kernel result are rendered in Fig. 6f-h. A complete isosurface rendering of filtering results can be referred to a digital supplement attached with this paper.

D. Quantitative Validation

1) 2-D Page Images: Among the above experiments, the page image belongs to a special application, where we are concerned more about the increasing identifiability of stripe numbers through the differential filtering. Therefore, the final counting accuracy obtained with the post-processing peak detection is a good quantitative index to evaluate the performance of various kernels. To give a statistical evaluation, we

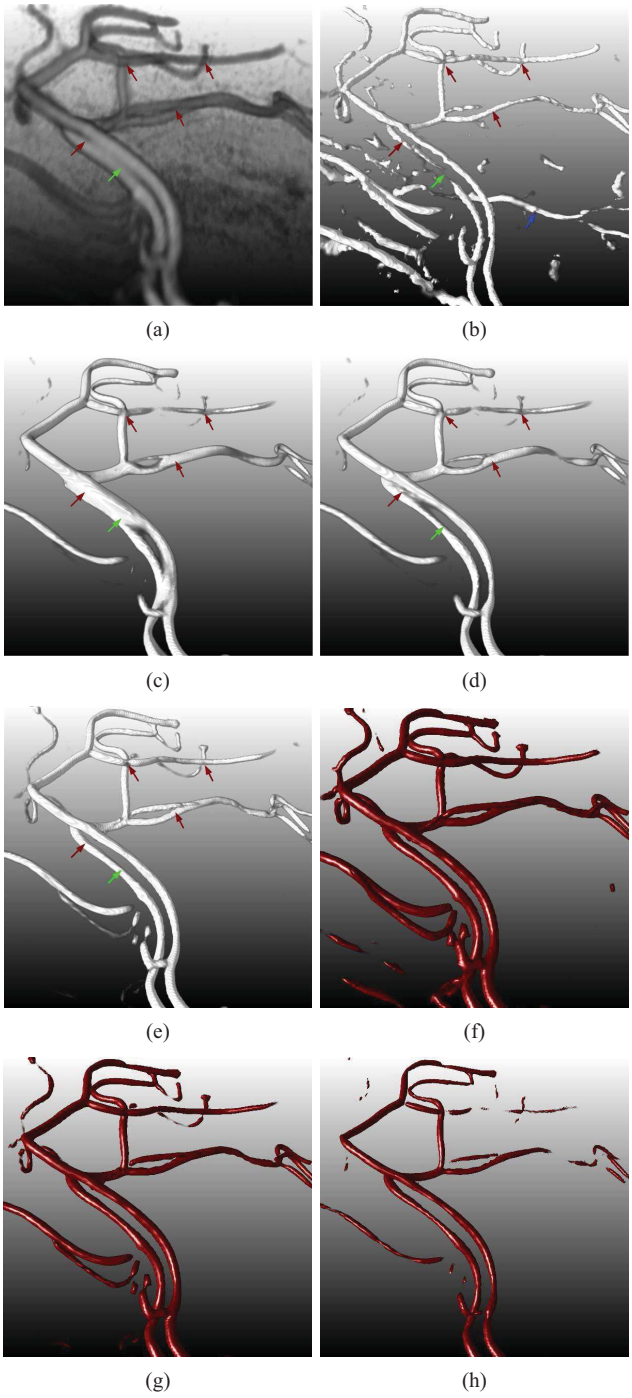

Fig. 6. 3-D clinical image filtered with different methods. (a)–(e) Image visualized with volume rendering. (f)–(h) Depiction of the isosurface rendering of the bi-Gaussian kernel result in (e) corresponding to different thresholds.

applied the five filters in Fig. 5 to 50 samples of stacked-sheets images, and over 400 profiles were chosen for statistical analysis. The page-counting errors are summarized in Table II. As shown, the Gaussian kernel, Laplace-Gabor and GVF filters commonly take negative biases, which means part of sheets were merged or missed. The rectangle kernel has a very high positive bias due to its large number of false responses. The bi-Gaussian kernel produced the lowest bias but with a larger variance than the Laplace-Gabor and GVF methods. It

TABLE II
STATISTICAL EVALUATION OF PAGE-COUNTING

Quantitative Indices	Gaussian Kernel	Rectangle Kernel	Bi-Gaussian Kernel	Laplace-Gabor	GVF
Systematic bias (%)	−0.723	16.570	**0.009**	−0.039	−0.048
Random error (%)	±4.253	±8.957	±2.123	±**1.193**	±1.417

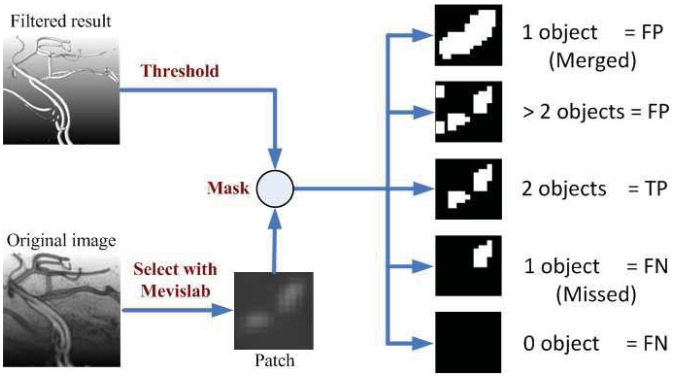

Fig. 7. Flowchart to evaluate vessel separation in MRA filtering.

indicates that the proposed bi-Gaussian kernel is more suitable for unbiased measurement, though a statistical averaging or other post-processing is necessary to reduce the non-ignorable random error. The Laplace-Gabor filter got the lowest variance, which can be indirectly verified from the smoother stripes in Fig. 5b.

2) 3-D Clinical Images: We randomly selected 15 volume images from the open dataset [37] containing clinical MRA data, and 18 pairs of adjacent vessels were manually selected using masks by two trained observers. As shown in Fig. 7, from these selected adjacent vessels, we chose patches in the planes approximately orthogonal to the vessel axes. Both the 2D cross-sections of neighboring vessels and the transition region between them were subsequently labeled manually. On average, there were about 120 patches drawn for each pair of vessels, resulting in a total of 2283 patches. The evaluation task was implemented in Mevislab [39], using the interactive contour editing and 2D-3D cursors synchronizing tools. The interactive segmentation was first performed by two trained operators, a third observer subsequently verified the editing result and a radiologist was enquired to settle the disputes. The sketched procedure circumvents the need to manually extract the whole vasculature, which is infeasible, and focuses the evaluation on adjacent vessels to demonstrate the separating ability of the several kernels.

To quantify the filtering performance, we first normalized the kernel responses to [0, 1]. When the normalized images are binarized with some global threshold, the isolation of neighboring vascular profiles across the patch plane will be a good index to evaluate the ability to separate adjacent structures. For each 2D patch, after thresholding the number of objects could be 0, 1, 2 or larger than 2, with 2 being the correct response. This can be more clearly understood from the

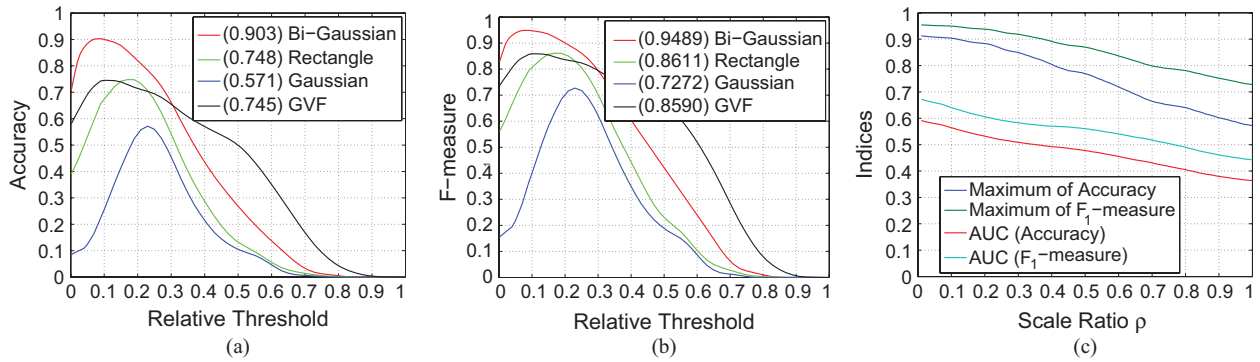

Fig. 8. Quantitative evaluation of 3-D vessel filters. (a) Accuracy and (b) F_1-measure curves, with legends showing the maximum responses. (c) Change of quantitative indices with the scale-ratio parameter of bi-Gaussian kernel and an offset of 0.2 is added to the two AUC curves for better display.

TABLE III
STATISTICAL EVALUATION OF 3-D VESSEL FILTERING

Method	Accuracy Maximum	Accuracy AUC	F_1-Measure Maximum	F_1-Measure
Bi-Gaussian kernel	**0.9028** (±0.0621)	0.3674 (±0.0852)	**0.9489** (±0.0338)	0.4339 (±0.0904)
Rectangle kernel	0.7480 (±0.1355)	0.2636 (±0.0649)	0.8558 (±0.0906)	0.3336 (±0.0745)
Gaussian kernel	0.5712 (±0.1241)	0.1639 (±0.0453)	0.7165 (±0.0949)	0.2317 (±0.0598)
GVF	0.7452 (±0.1246)	**0.4060** (±0.0950)	0.8539 (±0.0802)	**0.5072** (±0.0797)

*The statistical means are listed with their variances inside the brackets.

flowchart of Fig. 7, where the complete procedure is depicted. For the four different kinds of binarized responses inside a patch, the detection of zero objects corresponds to missing both vessels, while the case of a single object is caused by vessel merging or loss of a single branch. A count larger than 2 mainly arises from noise interference and false responses.

To perform the receiver operating characteristic (ROC) analysis for quantitative validation, we define a count 0 as a False Negative (FN), a count 2 as a True Positive (TP), and a count larger than 2 as False Positive (FP). A special case is a count 1, which can be classified as FP or FN depending whether the cause is merging or missing of objects, respectively. The accuracy is then equal to TP/(TP+FP+FN), where the True Negative (TN) is deliberately omitted due to the lack of a clear definition. Like the work of [27], we further used the F1-measure as a quantitative index, which is considered suitable for skewed data. It is defined as 2TP/(2TP+FP+FN). Note that both the accuracy and the F_1-measure are independent on the choice of FP or FN for the count 1 case.

The curves of accuracy and F_1-measure as a function of the relative threshold are given in Fig. 8a and b, respectively, which summarizes the results for all 2283 patches. In this experiment, the filtering parameters are set the same as Fig. 6, i.e. $\rho = 0.1$ for the bi-Gaussian kernel. As observed, the corresponding accuracy and F_1-measure curves take similar shapes. It is clear that the bi-Gaussian kernel has the highest maximum response among the four methods. The GVF model appears similar to the rectangle kernel filter in maximum responses, but obtains a wide coverage, which reflects its robustness to binarizing thresholds. More extensive evaluations are summarized in Table III. It can be found that the bi-Gaussian kernel obtains the highest mean maximum response under the lowest variance. The GVF takes the largest AUCs. With a proper selection of the threshold, the maximum response is the most important criterion for optimal vessel segmentation, at which the bi-Gaussian kernel is best.

E. Selection of Scale-Ratio Parameter in Bi-Gaussian Kernels

In Section III, we have briefly introduced the scale-ratio parameter configuration of the bi-Gaussian kernel. To verify its effect, we performed additional experiments using the MRA images, by adjusting ρ in the range (0, 1] with a step size of 0.01. The accuracy and F_1-measure responses of the bi-Gaussian kernel with varying configuration were then obtained, the four quantitative indices were calculated and the corresponding curves are illustrated in Fig. 8c. As shown, all the index curves are generally decreasing functions of ρ, though some small oscillations can be found. The two maximum response curves tend to be flat while $\rho < 0.1$, which means the filter is insensitive to the parameter inside this range. On the other hand, a too small ρ is at a risk to introduce background noise. In our experiments, the selection of $\rho \in [0.1, 0.2]$ appears a good compromise between optimization of maximum responses and immunity of noise interference.

F. Influence of Scale-Space Parameters

Among the previous derivative filters, there are several parameters including the minimum scale $\sigma_{\min}$, maximum scale $\sigma_{\max}$, scale step and normalizing coefficient γ, which need be configured for multi-scale integration. Usually, the $\sigma_{\max}$ and γ are considered the most sensitive parameters and should be chosen carefully.

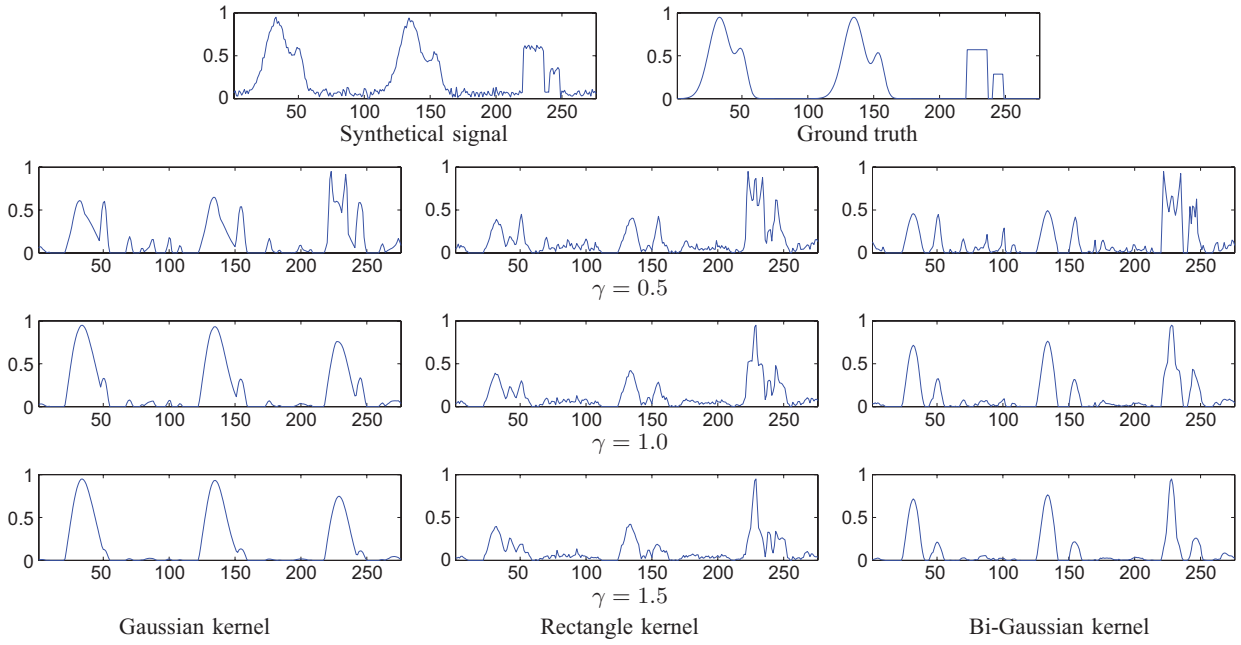

Fig. 9. Testing the sensitivity of parameter γ in different kernels with a 1-D synthetical signal.

Although the γ coefficient is theoretically optimized to 1 on basis of the scale-invariance criterion, it could be adjusted from other considerations. To verify the influence of γ to various line filters, a series of experiments were conducted with a noise-corrupted synthetical signal as shown in Fig. 9. Here, the Gaussian-like peaks are taken from Fig. 2a, and two neighboring bar-like peaks with radius 8 and 4 pixels are particularly added to simulate sharp profiles. The second-order derivatives of three different kernels are respectively convolved with the lD signal and generate the multi-scale responses under a common configuration $\sigma_{\min} = 2$, $\sigma_{max} = 10$ and step $= 1$ pixel. As observed, a large $\gamma > 1$ tends to create smoother results simultaneously at an increasing risk to merge close peaks, which is especially obvious with the Gaussian kernel. A small $\gamma < 1$ is beneficial to the separation of adjacent objects, but the drawback is to miss the bar-like peaks with large width or detect them incorrectly. Generally speaking, the default value $\gamma = 1$ keeps a better balance between noise-suppression and adjacent objection separation for all the three kernels. The bi-Gaussian kernel appears more robust to the γ parameter variation than the other two kernels.

The basic rule for $\sigma_{\max}$ configuration is to select its value just above the expected largest object size, but over- or under-estimation are very common in real applications. Like the results with $\gamma < 1$ in Fig. 9, a lower $\sigma_{\max}$ is better for separation of neighboring objects with Gaussian-like profiles, but will suffer from bar-like profiles and noise disturbance. In contrast, an over-large $\sigma_{\max}$ might blur the adjacent structures. As an example, the 3D clinic image in Fig. 6a is further filtered with $\sigma_{\max} = 5$ while the other parameters remain unchanged. Here, the interested vessel radii of original sub-volume fall between 1 and 3 pixels. As seen from the results in Fig. 10, the closely located vessels are seriously blurred under all the three filters, but the bi-Gaussian kernel has the smallest overlap of the results. Particularly, false vessel responses between the parallel tubes can be found in Fig. 10b, which means that the boundaries belonging to different vessels were erroneously identified as an object under the rectangle kernel.

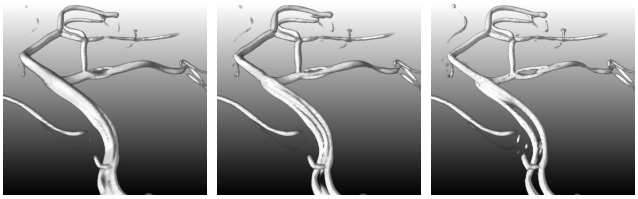

Fig. 10. Influence of an over-large $\sigma_{\max}$ in 3-D clinical image filtering. (a) Gaussian kernel. (b) Rectangular kernel. (c) Bi-Gaussian kernel.

VI. Conclusion

In this paper, a multi-scale derivative filter has been presented for the detection of adjacent curvilinear structures. Our idea was inspired by retrospection of traditional line filters. The classic Gaussian vesselness, gradient flux and medialness models are reformulated and uniformed into a differential convolution framework, which helps to better understand and further improve the existing methods. Our main contribution is to introduce the concept of scale separation on foreground and background. Based on this idea, a new bi-Gaussian filtering kernel is developed, which realized a natural integration of traditional Gaussian and rectangle (flux) kernels. With the deduction of its full analytical representation, the proposed kernel holds a potential ability to replace the low-level Gaussian operators in many vessel and structure detecting filters, especially concerning the specific

application of neighboring object extraction. To address the scale-normalization issue about non-Gaussian derivatives, our additional contribution is the design of several criteria based on response conservation to idealized standard signals.

The performance of our method was demonstrated in experiments by using synthetic and real images. It is shown that the proposed method is more effective in detecting adjacent structures compared with conventional filters. In particular, most tubular objects including those with mid-level overlap have been clearly separated while introducing few false responses. This is validated not only from the illustration of filtered results, but also with the quantitative accuracy and F_1-measure curves. For example, in the clinical image experiment, our method gained the highest maximum responses among the four kinds of filters, i.e. about 21% and 11% higher than the second best rectangle kernel on accuracy and F_1-measure maxima, respectively.

Compared with the Gaussian function, the proposed bi-Gaussian kernel essentially reduces adjacent disturbances with a shortened or sharpened tails. Although there exist probably countless functions to achieve the purpose, our kernel is a good choice in terms of clarity of physical meaning and easiness of normalization. However, a limitation of the bi-Gaussian kernel is that it is only differentiable up to the second-order, and it might be problematic if the image derivatives higher than two, such as the third-order edge strength measure [40], are required. In addition, the good structure separating property of our filtering kernel was obtained in the study with an assumption that the background noise of images is limited. Otherwise, we have to adopt a bigger scale ratio parameter to cancel this influence. In that case, our method will degrade to a traditional Gaussian filter.

Presently, our focus is on investigating the bi-Gaussian kernel as a general detector to extract reliable information from closely located structures. Strictly speaking, it only belongs to the category of feature detection or preprocessing enhancement. To deal with complicated tasks such as the separation of hepatic or pulmonary artery-vein trees, more specific segmentation schemes and additional constraints should be considered. For example, the current 3D operators might introduce unnecessary blurring orthogonal to the overlapping direction, which will probably decrease the discriminability of adjacent objects. The asymmetric intensity distribution is also frequently seen in many neighboring structures like blood vessels, and has not been sufficiently emphasized in the current work. These issues still remain an open problem and will be our future research direction.

Appendix A

Reformulation of the Gradient Flux Models

According to [19], the image gradient flux can be converted to a volume integral via the divergence theorem, i.e. $Flux(\sigma, x) = 1/S_R \int_R div(\nabla I) dR$, where R indicates the spherical neighborhood with radius σ and S_R its surface area. Notice this is actually a convolution of the Laplacian ΔI with the sphere function $R(\sigma, x)$, whose one-dimensional representation is a unit rectangle kernel. Further consider the noise-suppression Gaussian filtering with a small *constant* scale σ_b involved in gradient calculation, the gradient flux can be rewritten to

$$\begin{aligned} Flux(\sigma, x) &= \tfrac{1}{S_R} \int_R div(\nabla I_{\sigma_b}) dR \\ &= \tfrac{V_R}{S_R} \cdot div[I(x) * \nabla G(\sigma_b, x)] * \bar{R}(\sigma, x) \end{aligned} \tag{A1}$$

where the normalized kernel $\bar{R}(\sigma, x)$ is obtained from $R(\sigma, x)$ divided by its volume integral V_R. The coefficient $V_R/S_R \propto \sigma$, and σ is used for simplification. In fact, it resembles a traditional scale-normalizing term. Thus, according to the differential property of convolution, we have

$$Flux(\sigma, x) = \sigma \cdot I(x) * \Delta \bar{R}(\sigma, \sigma_b, x) \tag{A2}$$

with $\bar{R}(\sigma, \sigma_b, x) = G(\sigma_b, x) * \bar{R}(\sigma, x)$ being a smoothened rectangle function.

The OOF model of Law and Chung [20] adopted the second-order partial differentials of $\bar{R}(\sigma, \sigma_b, x)$, namely DoRs, to construct Hessian matrix, see Eq. (3). To further understand the DoR operators, their 1D analytical representations can be obtained with the distributional derivative of Heaviside step functions, i.e. $\partial \bar{R}(\sigma, \sigma_b, x)/\partial x = 1/2\sigma \cdot [G(\sigma_b, x + \sigma) - G(\sigma_b, x - \sigma)]$ and $\partial^2 \bar{R}(\sigma, \sigma_b, x)/\partial x^2 = 1/2\sigma \cdot [G'(\sigma_b, x+\sigma) - G'(\sigma_b, x-\sigma)]$. Obviously, the terms are the combination of two shifted Gaussians and their first-order derivatives, respectively.

Appendix B

Reformulation of the Medialness Function

In [10], the 2D medialness response was originally defined as $M(\sigma_b, x) = 1/2\pi \int_0^{2\pi} -\sigma_b^{\gamma} \cdot \nabla I_{\sigma_b}(x + \tau\sigma_b \vec{v}_\alpha) \cdot \vec{v}_\alpha d\alpha$. Here, $\vec{v}_\alpha = cos(\alpha)\vec{e_1} + sin(\alpha)\vec{e_2}$ is the unit vector in radial directions across the transverse plane defined by $\vec{e_1}$ and $\vec{e_2}$. The term σ_b^{γ} is added on purpose for scale-normalization of gradient calculation, and the parameter τ ensures the circle radius $\sigma = \tau\sigma_b$. Thus, the central Hessian and its eigenvectors are computed at scale σ, whereas the boundary gradient at σ_b like the flux models. Obviously, $M(\cdot)$ is the average of gradient projections taken in radial directions around a circle C_σ. Then, the medialness can be rewritten as a flux-like representation:

$$\begin{aligned} M(\sigma, \sigma_b, x) &= \frac{1}{2\pi\sigma} \sigma_b^{\gamma} \int_{C_\sigma} < \nabla I_{\sigma_b}, \vec{n} > ds \\ &= \tfrac{1}{2} \rho^{\gamma} \sigma^{\gamma+1} \cdot I(x) * \Delta \bar{R}^c(\sigma, \sigma_b, x) \end{aligned} \tag{B1}$$

where $\rho = \sigma_b/\sigma$, R^c denotes the planar region surrounded by circle C_σ and its 1D representation is also a unit rectangle function. $\bar{R}^c$ corresponds to R^c divided by its area $\pi\sigma^2$, then $\bar{R}^c(\sigma, \sigma_b, x) = \bar{R}^c(\sigma, x) * G(\sigma_b, x)$ is a 2D smoothened rectangle kernel through the transverse plane. Since the term $1/2\rho^{\gamma}$ is constant, it can be omitted for simplification.

Appendix C

Scale Normalization of the Rectangle Kernels

As introduced in Section II, the zero-order smoothened rectangle kernel is defined as $\bar{R}(\sigma, \sigma_b, x) = 1/2\sigma G(\sigma_b, x) * [u(x + \sigma) - u(x - \sigma)]$ with the term $1/2\sigma$ to ensure constant

conservation. Then, using NF_1^r to represent the first-order normalizing factor, the positive half integral of $\bar{R}'(\sigma, \sigma_b, x)$ is written as

$$A_1^r = -\int_0^{+\infty} NF_1^r(\sigma) \cdot \bar{R}'(\sigma, \sigma_b, x)dx = \frac{1}{2\sigma} NF_1^r(\sigma) \cdot erf(\frac{\sigma/\sigma_b}{\sqrt{2}}). \quad \text{(C1)}$$

By step conservation, we set $NF_1^r(\sigma) = \sigma$ to guarantee A_1^r being constant on condition that $\sigma_b \ll \sigma$ or the ratio $\rho = \sigma_b/\sigma$ is fixed.

As for the second-order kernel, the positive half integral is obtained as

$$A_2^r = -\int_{-\sigma}^{\sigma} NF_2^r(\sigma) \cdot \bar{R}''(\sigma, \sigma_b, x)dx = \frac{1}{\sigma} NF_2^r(\sigma) \cdot \frac{1}{\sigma_b\sqrt{2\pi}} \left[1 - \exp(-\frac{2\sigma^2}{\sigma_b^2})\right] \quad \text{(C2)}$$

with $NF_2^r(\sigma)$ the normalizing coefficient. If $\sigma_b \ll \sigma$, Eq. (C2) is approximated to $A_r^2 \approx 1/\sigma NF_2^r(\sigma) \cdot 1/\sigma_b\sqrt{2\pi}$. Then, fixing the value of σ_b, $NF_2^r = \sigma$ is able to keep A_2^r a constant. On the other hand, if the ratio $\rho = \sigma_b/\sigma$ is fixed, by rewriting Eq. (C2) to $A_2^r = 1/\sigma^2 NF_2^r(\sigma) \cdot 1/\sqrt{2\pi}1/\rho\left[1 - \exp(-2/\rho^2)\right]$, it is obvious that NF_2^r should be chosen to σ^2. Actually, the two cases represent different scale-normalization schemes for rectangle kernel related operators. The former corresponds to the flux filters [19], and the gradient scale σ_b is fixed to 1 pixel in the OOF model [20]. The latter is the case of medialness filters [9], [10], where σ_b is proportional to the object scale σ.

ACKNOWLEDGMENT

The MR brain images from healthy volunteers used in this paper were collected and made available by the CASILab at The University of North Carolina, Chapel Hill, and were distributed by the MIDAS Data Server at Kitware, Inc., Clifton Park, NY.

REFERENCES

[1] I. Sluimer, A. Schilham, M. Prokop, and B. V. Ginneken, "Computer analysis of computed tomography scans of the lung," *IEEE Trans. Med. Imag.*, vol. 25, no. 4, pp. 385–405, Apr. 2006.

[2] R. D. Young, R. J. Reed, and F. H. Crosdale, "Apparatus and method for counting sheets," E.P. Patent 0 743 616, Jun. 6, 1996.

[3] D. Lesage, E. D. Angelini, I. Bloch, and G. Funka-Lea, "A review of 3D vessel lumen segmentation techniques: Model, features and extraction schemes," *Med. Image Anal.*, vol. 13, no. 6, pp. 819–845, 2009.

[4] T. M. Koller, G. Gerig, G. Szekely, and D. Dettwiler, "Multiscale detection of curvilinear structures in 2-D and 3-D image data," in *Proc. 5th Int. Comput. Vis. Conf.*, 1995, pp. 864–869.

[5] G. Agam, S. G. I. Armato, and C. Wu, "Vessel tree reconstruction in thoracic CT scans with application to nodule detection," *IEEE Trans. Med. Imag.*, vol. 24, no. 4, pp. 486–499, Apr. 2005.

[6] C. Lorenz, I. C. Carlsen, T. M. Buzug, C. Fassnacht, and J. Weese, "Multiscale line segmentation with automatic estimation of width, contrast and tangential direction in 2D and 3D medical images," in *Proc. 1st Joint Conf. Comput. Vis. Virtual Rel. Robot. Med. Medial Robot. Comput.-Assist. Sur.*, 1997, pp. 233–242.

[7] Y. Sato, S. Nakajima, N. Shiraga, H. Atsumi, S. Yoshida, T. Koller, G. Gerig, and R. Kikinis, "Three-dimensional multiscale line filter for segmentation and visualization of curvilinear structures in medical images," *Med. Image Anal.*, vol. 2, no. 2, pp. 143–168, 1998.

[8] A. F. Frangi, W. J. Niessen, K. L. Vincken, and M. A. Viergever, "Multiscale vessel enhancement filtering," in *Proc. Med. Image Comput. Comput.-Assist. Interv.*, 1998, pp. 130–137.

[9] S. M. Pizer, D. Eberly, D. S. Fritsch, and B. S. Morse, "Zoom-invariant vision of figural shape: The mathematics of cores," *Comput. Vis. Image Understand.*, vol. 69, no. 1, pp. 55–71, 1998.

[10] K. Krissian, G. Malandain, N. Ayache, R. Vaillant, and Y. Trousset, "Model-based detection of tubular structures in 3D images," *Comput. Vis. Image Understand.*, vol. 80, no. 2, pp. 130–171, 2000.

[11] T. Lindeberg, "Feature detecion with automatic scale selecion," *Int. J. Comput. Vis.*, vol. 30, no. 2, pp. 79–116, 1998.

[12] M. J. McAuliffe, D. Eberly, D. S. Fritsch, E. L. Chaney, and S. M. Pizer, "Scale-space boundary evolution initialized by cores," in *Proc. 4th Int. Conf. Vis. Biomed. Comput.*, 1996, pp. 173–182.

[13] T. Pock, R. Beichel, and H. Bischof, "A novel robust tube detection filter for 3D centerline extraction," in *Proc. 14th Scandin. Conf. Image Anal.*, 2005, pp. 481–490.

[14] C. Bauer, T. Pock, E. Sorantin, H. Biscof, and R. Beichel, "Segmentation of interwoven 3D tubular tree structures utilizing shape priors and graph cuts," *Med. Image Anal.*, vol. 14, no. 2, pp. 172–184, 2010.

[15] P. Perona and J. Malik, "Scale-space and edge detection using anisotropic diffusion," *IEEE Trans. Pattern Anal. Mach. Intell.*, vol. 12, no. 7, pp. 629–639, Jul. 1990.

[16] J. Weickert, "A review of nonlinear diffusion filtering," in *Proc. Scale-Space Theory Comput. Vis. Conf.*, 1997, pp. 3–28.

[17] C. Bauer and H. Bischof, "A novel approach for detection of tubular objects and its application to medical image analysis," in *Proc. Symp. Pattern Recognit. Conf.*, 2008, pp. 163–173.

[18] C. Xu and J. L. Prince, "Snakes, shapes, and gradient vector flow," *IEEE Trans. Image Process.*, vol. 7, no. 3, pp. 359–369, Mar. 1998.

[19] A. Vasilevskiy and K. Siddiqi, "Flux maximizing geometric flows," *IEEE Trans. Pattern Anal. Mach. Intell.*, vol. 24, no. 12, pp. 1565–1578, Dec. 2002.

[20] M. W. Law and A. C. Chung, "Three dimensional curvilinear structure detection using optimally oriented flux," in *Proc. Eur. Conf. Comput. Vis.*, 2008, pp. 368–382.

[21] M. W. Law and A. C. S. Chung, "An oriented flux symmetry based active contour model for three dimensional vessel segmentation," in *Proc. Comput. Sci. Vis. Conf.*, 2010, pp. 720–734.

[22] F. Benmansour and L. D. Cohen, "Tubular structure segmentation based on minimal path method and anisotropic enhancement," *Int. J. Comput. Vis.*, vol. 92, no. 2, pp. 192–210, 2011.

[23] H. Knutsson and C.-F. Westin, "Normalized and differential convolution: Methods for interpolation and filtering of incomplete and uncertain data," in *Proc. Comput. Vis. Pattern Recognit. Conf.*, 1993, pp. 515–523.

[24] A. Witkin, "Scale space filtering," in *Proc. Int. Joint Conf. Artif. Intell.*, 1983, pp. 1019–1023.

[25] J. J. Koenderink, "The structure of images," *Biol. Cybern.*, vol. 50, no. 5, pp. 363–370, 1984.

[26] D. S. Fritsch, S. M. Pizer, B. S. Morse, D. H. Eberly, and A. Liu, "The multiscale medial axis and its applications in image registration," *Pattern Recognit. Lett.*, vol. 15, no. 5, pp. 445–452, 1994.

[27] R. Estrada, C. Tomasi, M. Cabrera, D. Wallace, S. Freedman, and S. Farsiu, "Exploratory Dijkstra forest based automatic vessel segmentation: Applications in video indirect ophthalmoscopy (VIO)," *Biomed. Opt. Exp.*, vol. 3, no. 2, pp. 327–339, 2012.

[28] T. Lindeberg, "Scale-space for discrete signals," *IEEE Trans. Pattern Anal. Mach. Intell.*, vol. 12, no. 3, pp. 234–254, Mar. 1990.

[29] L. M. Florack, B. M. Romeny, J. J. Koenderink, and M. A. Viergever, "Scale and the differential structure of images," *Image Vis. Comput.*, vol. 10, no. 6, pp. 376–388, 1992.

[30] E. J. Pauwels, L. J. Gool, P. Fiddenlaers, and T. Moons, "An extended class of scale-invariant and recursive scale space filters," *IEEE Trans. Pattern Anal. Mach. Intell.*, vol. 17, no. 7, pp. 691–701, Jul. 1995.

[31] Q. Lin, "Enhancement, extraction, and visualization of 3D volume data," Ph.D. dissertation, Dept. Electr. Eng., Linkoping Univ., Linkoping, Sweden, 2003.

[32] A. K. Jain, *Fundamentals of Digital Image Processing*. Upper Saddle River, NJ: Prentice-Hall, 1989.

[33] C. Xiao, M. Staring, D. P. Shamonin, J. H. C. Reiber, J. Stolk, and B. C. Stoel, "A strain energy filter for 3D vessel enhancement with application to pulmonary CT images," *Med. Image Anal.*, vol. 15, no. 1, pp. 112–124, 2011.

[34] M. W. Law and A. C. Chung, "Efficient implementation for spherical flux computation and its application to vascular segmentation," *IEEE Trans. Image Process.*, vol. 18, no. 3, pp. 596–612, Mar. 2009.

[35] B. M. Westling and G. T. Nilsson, "Apparatus for counting sheets lying on each other in a stack," E.P. Patent 9 100 014, Jul. 25, 1991.
[36] P. Du, W. Kibbe, and S. Lin, "Improved peak detection in mass spectrum by incorporating continuous wavelet transform-based pattern matching," *Bioinformatics*, vol. 22, no. 17, pp. 2059–2065, 2006.
[37] E. Bullitt, D. Zeng, G. Gerig, S. Aylward, S. Joshi, J. K. Smith, W. Lin, and M. G. Ewend, "Vessel tortuosity and brain tumor malignancy: A blinded study," *Acad. Radiol.*, vol. 12, no. 10, pp. 1232–1240, 2005.
[38] K. Krissian, R. Kikinis, and C. Westin, "Algorithms for extracting vessel centerlines," Dept. Radiol., Harvard Medial School, Boston, MA, Tech. Rep. 0003, Sep. 2004.
[39] I. Bitter, R. V. Uitert, I. Wolf, L. Ibanez, and J. M. Kuhnigk, "Comparison of four freely available frameworks for image processing and visualization that use ITK," *IEEE Trans. Vis. Comput. Graph.*, vol. 13, no. 3, pp. 483–493, May 2007.
[40] T. Lindeberg, "Edge detection and ridge detection with automatic scale selection," *Int. J. Comput. Vis.*, vol. 30, no. 2, pp. 117–154, 1998.

Changyan Xiao received the M.S. degrees in mechanical and electronic engineering from the National University of Defense Technology, Changsha, China, and the Ph.D. degree in biomedical engineering from Shanghai Jiaotong University, Shanghai, China, in 1997 and 2005, respectively.

He was a Visiting Post-Doctoral Researcher with the Division of Image Processing, Leiden University Medical Center, Leiden, The Netherlands, from 2008 to 2009. Since 2005, he has been with the College of Electrical and Information Engineering, Hunan University, Changsha. His current research interests include vessel detection and pulmonary structure segmentation in medical imaging.

Marius Staring received the M.Sc. degree in applied mathematics from the University of Twente, Enschede, The Netherlands, and the Ph.D. degree in medical image registration from UMC Utrecht, Utrecht, The Netherlands, in 2002 and 2008, respectively.

He has been with the Division of Image Processing, Leiden University Medical Center, Leiden, The Netherlands, since 2008. He has co-authored with Dr. S. Klein the registration package *Elastix*. His current research interests include image registration and (pulmonary) image processing.

Yaonan Wang received the M.S. and Ph.D. degrees in electrical engineering from Hunan University, Changsha, China, in 1990 and 1994, respectively.

He was a Senior Humboldt Fellow in Germany from 1998 to 2000, and he was a Visiting Professor with the University of Bremen, Bremen, Germany, from 2001 to 2004. He has been with Hunan University since 1995, where he is currently a Professor. His current research interests include intelligent control and information processing, machine vision, and robot and industrial process control.

Denis P. Shamonin received the Master's degree in applied mathematics St. Petersburg State Marine Technical University, St. Petersburg, Russia, in 2002.

He was a Scientific Programmer with the Section of Computational Science, University of Amsterdam, The Netherlands. He has been a Scientific Programmer with the Division of Image Processing, Leiden University Medical Center, Leiden, The Netherlands, since 2005. His current research interests include pulmonary image processing and quantification, visualization, and analysis algorithms for clinical applications.

Berend C. Stoel received the M.Sc. degree in medical informatics from Leiden University, Leiden, The Netherlands, and the Ph.D. degree in objective assessment of X-ray image quality from Leiden University Medical Center (LUMC), Leiden, in 1989 and 1996, respectively.

He is currently an Assistant Professor with the Division of Image Processing, Department of Radiology, LUMC, where he is the Head of the Section of Orthopaedics and Pulmonology. His current research interests include pulmonology, particularly quantification of emphysema, pulmonary fibrosis and embolisms, and bronchial tree quantification, with a focus on the clinical validation and applications in drug evaluation trials.